*At the crossroads of astrophysics and cosmology: Period–luminosity relations in the 2020s*
*Proceedings IAU Symposium No. 376, 2024*
*R. de Grijs, P. A. Whitelock & M. Catelan, eds.*
doi:10.1017/S1743921323002685

# The Tip of the Red Giant Branch as a Cosmological Tool

**Myung Gyoon Lee**

Seoul National University, Department of Physics and Astronomy, SNUARC, Seoul, Republic of Korea. email: mglee@astro.snu.ac.kr

**Abstract.** The luminosity of the brightest stars (tip) of the red giant branch (TRGB) in the color–magnitude diagrams of old stars was used early on to introduce the 'multiple stellar populations' concept, in 1944, by Walter Baade. However, the precision and accuracy of the TRGB for distance estimation has not been known well for long. In the modern era, equipped with high spatial resolution imaging telescopes, the TRGB is considered an excellent standard candle for any type of resolved galaxies, thus representing a powerful probe for cosmology. The TRGB has several advantages over the classical Cepheids. I review how we can apply the TRGB in cosmology. Four science cases, from large to small scales, are presented: (1) the Hubble flow with Type Ia supernovae; (2) Virgo Cluster infall and dark matter; (3) dark galaxies; and (4) dark matter-free galaxies.

**Keywords.** Cosmology, Cosmic distance scale, Dark matter, Galaxies, Galaxy clusters

## 1. Introduction

Cepheids are great! Cepheids have become popular as the best standard candle for resolved galaxies. Period–luminosity relations of Cepheids (Leavitt's law) opened a new era of extragalactic astronomy and observational cosmology, one of the main topics of this symposium (see the reviews by Freedman and Riess in these proceedings).

However, Cepheids are found only in late-type galaxies, while the Universe is composed not only of late-type galaxies but also includes early-type galaxies; see Figure 1. We need a comparable standard candle that covers both late-type and early-type galaxies in the local Universe. That standard candle is the tip of the red-giant branch (TRGB) (Lee et al. 1993; Beaton et al. 2019; Madore et al. 2023, and references therein). Here, I introduce some examples of cosmological applications of the TRGB. I present some science cases, from large to small scales: (1) the Hubble flow with Type Ia Supernovae (SNe Ia); (2) Virgo Cluster infall and dark matter; (3) dark galaxies; and (4) dark matter-free galaxies.

## 2. What is the TRGB?

The TRGB is the brightest part of the red giant branch (RGB) in the color–magnitude diagrams (CMDs) of old stars in stellar systems such as galaxies or globular clusters. Theoretically, it corresponds to the core-helium flash stage in the evolution of low-mass stars in the Hertzsprung–Russell (HR) diagrams. Figure 2 (left) displays the conventional $M_V, (B-V)$ CMD of M55, a Milky Way globular cluster, and Figure 2 (right) shows the composite $M_I, (V-I)$ CMD of 46 Milky Way globular clusters (Freedman 2021). The $M_V, (B-V)$ CMD of M55 clearly shows the TRGB. The $V$-band magnitude of the TRGB varies significantly, depending on the metallicity. However, the TRGB's $I$-band magnitude, shown in Figure 2 (right), is much less metallicity-dependent so that it can be used as a precise standard candle. Photographic magnitudes of the TRGB

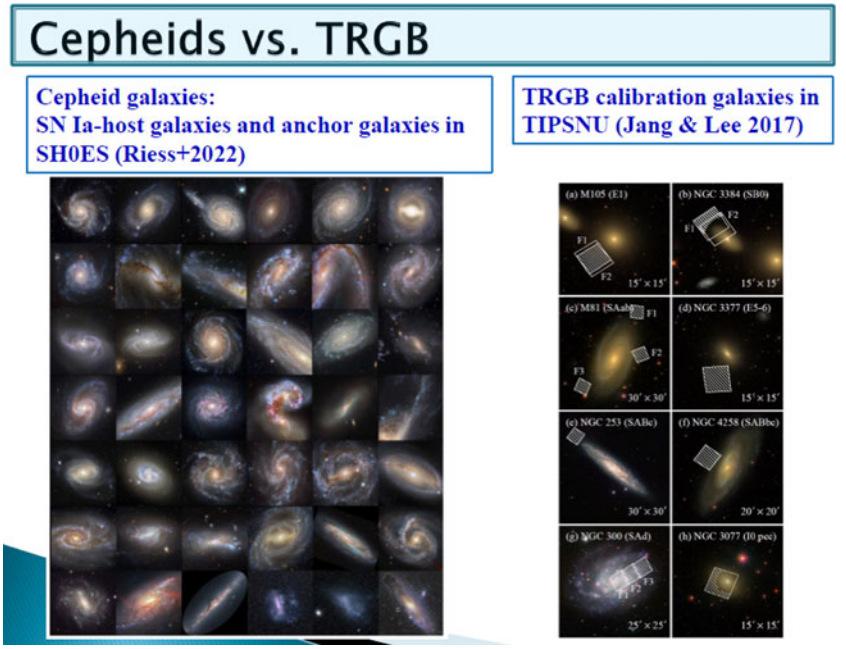


**Figure 1.** Morphological types of sample galaxies where, respectively, Cepheids (Riess et al. 2022, left) and the TRGB (Jang & Lee 2017a, right) have been used for distance measurements.

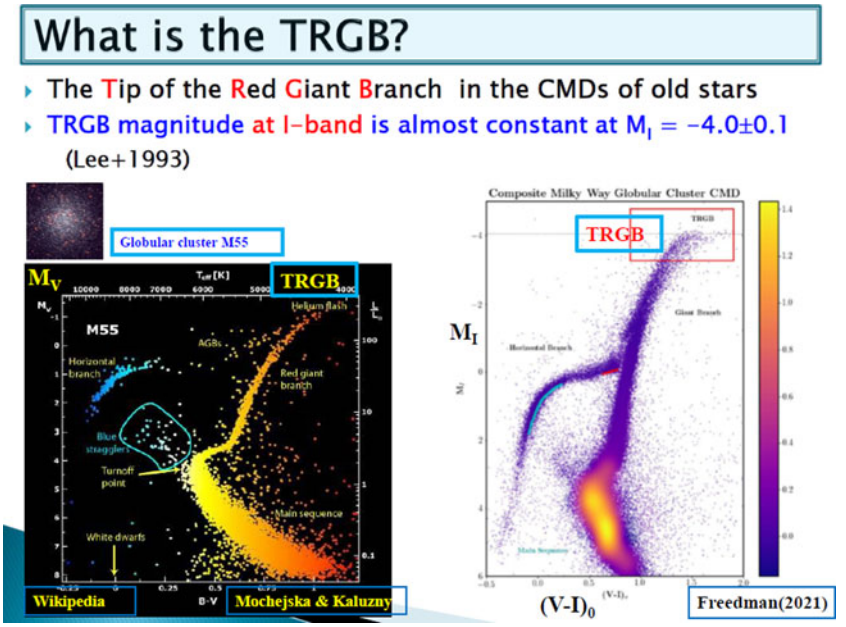


**Figure 2.** (left) $M_V, (B-V)$ CMD of the Milky Way globular cluster M55 (Mochejska and Kaluzny, via Wikipedia). (right) Composite $M_I, (V-I)$ CMD of 46 Milky Way globular clusters (Freedman 2021).

https://doi.org/10.1017/S1743921323002685 Published online by Cambridge University Press

were used to introduce the concept of Populations I and II in M31 and its companion galaxies as early as 1944 by Walter Baade. Thereafter, the TRGB was sometimes used for distance estimation to nearby galaxies but its reliability has not been known well for long. Only in 1993 it was shown that the TRGB is an excellent standard candle, comparable to Cepheids (Lee et al. 1993; Lee 1993). The limit of the TRGB for distance measurement used to be about 3 Mpc based on ground-based observations, but that distance scale increased by a factor of 10 with the advent of the *Hubble Space Telescope* (*HST*), reaching about 30 Mpc today (Jang & Lee 2017a,b).

### 2.1. *TRGB vs. Cepheids*

Almost all galaxies in the local Universe were formed at early times. Not only typical elliptical and lenticular galaxies but also star-forming irregular/spiral galaxies host old stellar populations with ages older than a few giga-years. As such, the TRGB method can be applied to any type of resolved galaxies in the local Universe, while the Cepheid method can be applied only to the late-type, resolved galaxies. Old RGB stars are best visible in the halo of a galaxy, while Cepheids are located in star-forming regions in galaxy disks. Thus, the TRGB based on halo stars is almost free of internal extinction. In contrast, Cepheids suffer significantly from the internal extinction problem. To reduce this problem, Wesenheight relations (which are defined to be reddening-free) have been designed. In addition, the *I*-band TRGB magnitude varies little in the low-metallicity regime where most TRGB measurements are obtained. The TRGB magnitude is fainter than the Cepheid magnitudes in optical bands, but it becomes brighter in near- and mid-infrared bands, which cover the main window of the *James Webb Space Telescope* (*JWST*).

Today, the number of the galaxies with the TRGB distances has reached more than 500, which is about eight times larger than the number of Cepheid distances (Jang & Lee 2017b; Anand et al. 2021; Tully et al. 2023; Madore et al. 2023). This ratio is expected to increase significantly in the near future. This shows clearly that the TRGB is a more versatile tool for cosmology than the use of Cepheids.

### 2.2. *Methods for the TRGB Estimation*

Figure 3 shows an example galaxy for TRGB measurements, NGC 4592, a dwarf spiral galaxy located in front of the Virgo Cluster. We chose, as an example, this spiral galaxy rather than an early-type galaxy, because the CMDs of late-type galaxies are more complicated than those of early-type galaxies. Kim et al. (2020) used *HST*/Wide-Field Camera 3 (WFC3) F555W/F814W images of this galaxy from the archive. The middle panel shows a gray-scale map of the F814W image of this galaxy, the location of which is marked in the color map of the Subaru/HyperSuprime Cam images in the left panel. The right panel shows a F814W, (F555W − F184W) CMD of the measured stars in the off-disk region marked in the middle panel. The red dots in the middle panel denote the RGB star candidates selected from the CMD of the detected stars. Various stellar populations are visible: blue supergiants as well as bright main-sequence stars, red supergiants, RGB stars, and asymptotic giant-branch (AGB) stars. The most notable feature is the thick RGB. The stars in this RGB mainly belong to the old halo, while the other stars are mostly drawn from the young disk. The bright top of the RGB is distinguishable at F814W $\sim$ 25.8 mag, clearly showing the location of the TRGB.

The principle adopted for typical TRGB magnitude measurements is simple: we detect a significant jump in the luminosity functions (LFs) of the RGB star candidates selected from the CMDs of resolved stars, and we measure the magnitude of the jump. The jump is primarily due to the high number ratio of RGB and AGB stars in old stellar systems,

https://doi.org/10.1017/S1743921323002685 Published online by Cambridge University Press

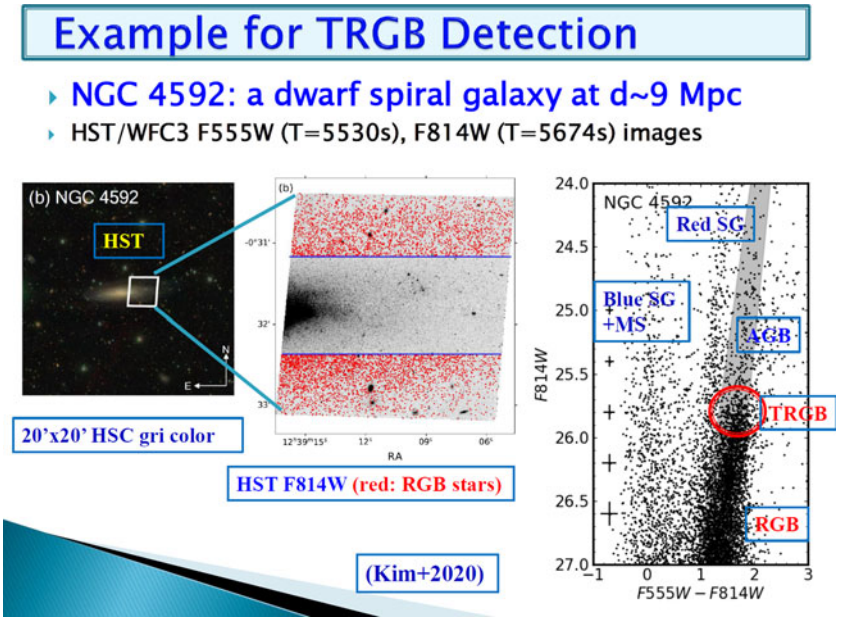


**Figure 3.** Example of a TRGB measurement: NGC 4592 (Kim et al. 2020). (left) Location of the *HST* field (white box) marked in pseudo-color Subaru/Hypersuprime Cam images of NGC 4592. (middle) Gray-scale map of the F814W image of the *HST* field. The outer regions in the halo of NGC 4592 were used for selection of the RGB star candidates (marked with red dots). (right) F814W, (F555W − F184W) CMD of the detected stars in the outer regions of the *HST* field. Various stellar populations are labeled. The red circle denotes the location of the TRGB. Plus signs on the left represent mean photometric errors for a given magnitude.

as shown in stellar evolution models. In optical bands, the $I$ (or F814W) band is best for TRGB measurements, because the TRGB magnitude of low-metallicity RGB stars is almost constant in this band (Lee et al. 1993; Jang & Lee 2017a).

In the CMD of RGB stars spanning a large range in metallicity, the TRGB is represented by a line following the upper edge of the RGB. This upper edge (locus) of the RGB is almost horizontal in the $I$, $(V - I)$ CMDs. Therefore, we apply an edge detection algorithm to detect the TRGB in the LFs.

Typical methods to measure the TRGB are briefly summarized in Kim et al. (2020), as follows: (a) direct edge detection (DED) with a Sobel filter (Lee et al. 1993; Jang & Lee 2017a); (b) GLOESS (Gaussian windowed, locally weighted scatterplot smoothing) edge detection (GED) for smoothed LFs (Hatt et al. 2017); and (c) maximum-likelihood (ML) LF fitting with a model LF of RGB and AGB stars (Méndez et al. 2002; Makarov et al. 2006).

### 2.3. *Precision of the TRGB*

We check the precision of the TRGB using a comparison of measurements based on multiple methods. Figure 4 compares the TRGB magnitudes for NGC 4592 as measured using the three methods described above. The TRGB magnitudes from all three methods show excellent agreement at the level of ±0.01 mag. On this basis, Kim et al. (2020) derived a distance to this galaxy of $d = 9.07 \pm 0.27$ Mpc. The typical precision of TRGB magnitude measurements with good data is ±0.02–0.03 mag (corresponding to a distance error of 1–1.5%). The TRGB magnitude measurement error can be as large as ±0.1 mag for difficult cases (corresponding to a distance error of 5%).

https://doi.org/10.1017/S1743921323002685 Published online by Cambridge University Press

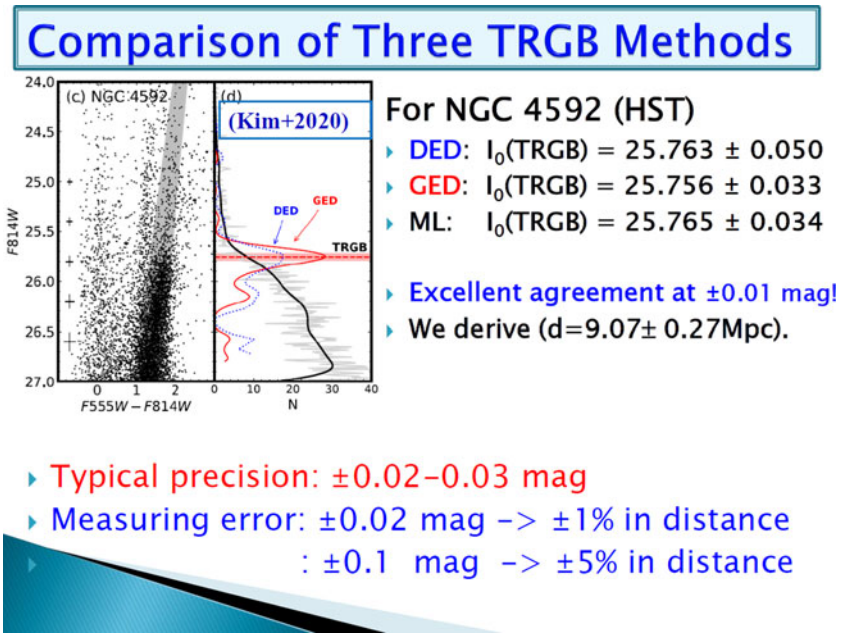


**Figure 4.** Comparison of TRGB magnitude measurements for NGC 4592 derived from three methods applied to the LF of the RGB stars (black line): direct edge detection (DED; blue line); GLOESS edge detection (GED; red line); and maximum-likelihood LF fitting with model LFs (ML) (Kim et al. 2020).

### 2.4. *Accuracy of the TRGB*

The accuracy of the TRGB depends mainly on the calibration error of the absolute magnitude of the TRGB. Calibration of the $I$-band magnitude of the TRGB was originally based on RR Lyrae (or the horizontal branch, HB; see Lee et al. 1993, and references therein). However, modern calibration of the TRGB (as well as for Cepheids) is based on geometric distance anchors (primary distance indicators), including detached eclipsing binaries in nearby galaxies (LMC, SMC), water megamasers in nearby galaxies (NGC 4258/M106), and parallaxes (*Gaia* stars in the Milky Way).

Figure 5 displays a comparison of TRGB loci in the $M_I$, $(V-I)$ diagram derived from observations (Lee et al. 1993; Rizzi et al. 2007; Madore et al. 2009; Jang & Lee 2017a; Freedman et al. 2020; Jang et al. 2021; Li et al. 2022; Soltis et al. 2021; Hoyt 2023) and theoretical models (Salaris & Cassisi 1997; Bellazzini 2008; Serenelli et al. 2017). Most calibrations show good agreement for the low-metallicity range ([Fe/H] $< -1$ dex). Note that the TRGB locus of Jang & Lee (2017a) was derived from a combination of eight nearby galaxies of diverse morphological types, covering a wide range of color. At this TRGB locus, the $I$-band TRGB magnitude is almost constant for the blue color range (i.e., for low metallicity, [Fe/H] $< -1$ dex), but it becomes fainter as the color increases (i.e., for higher metallicity). The blue region of the TRGB loci is mainly used for galaxy distance estimation, because most of the resolved stars in galaxy halos have low metallity ([Fe/H] $< -1$ dex).

In Figure 6, we display a zoomed-in view of the TRGB loci of two low-mass galaxies, the LMC and the SMC, recently derived by Hoyt (2023). It can be seen that the TRGB loci of these two galaxies are in excellent agreement with that derived from the combined sample of eight galaxies of Jang & Lee (2017b) (with updated zero points). Note that this latter TRGB locus exhibit a significant difference in the red color compared with the TRGB locus given by Rizzi et al. (2007).

https://doi.org/10.1017/S1743921323002685 Published online by Cambridge University Press

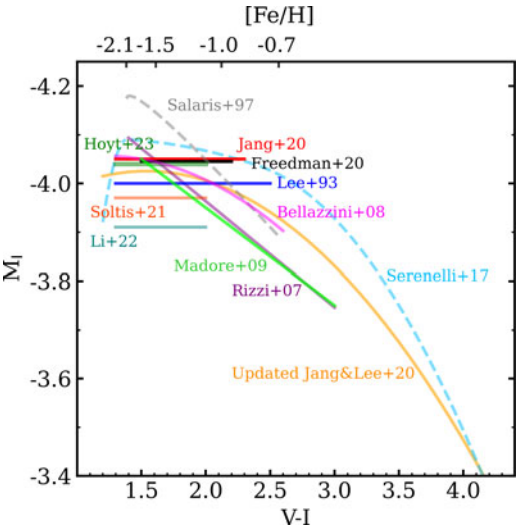


**Figure 5.** Comparison of the TRGB loci in the $M_I, (V-I)$ CMD derived from observations and theoretical models from the literature. Horizontal lines denote only the constant magnitudes for the low-metallicity range, which are generally used for distance estimation.

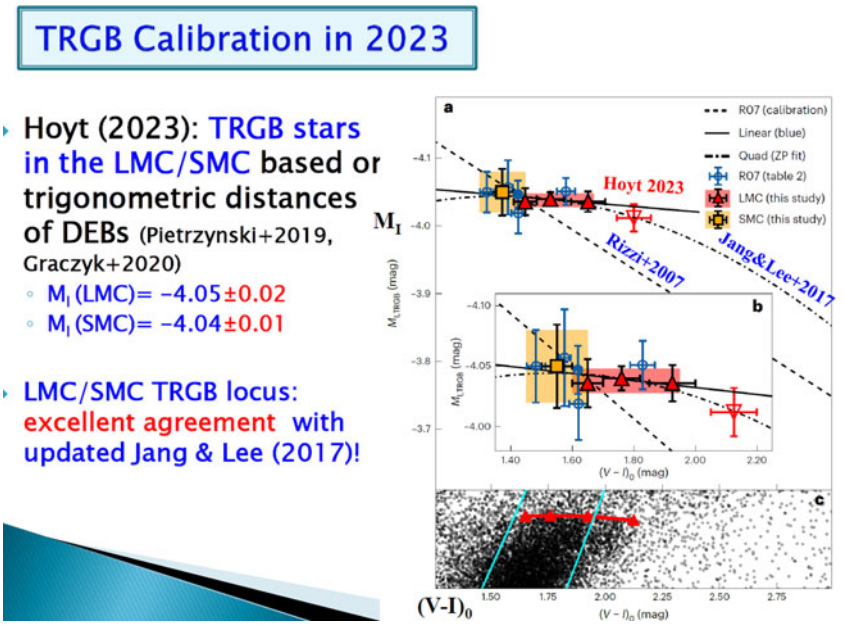


**Figure 6.** TRGB loci in the LMC (red symbols) and SMC (yellow symbols) in the $M_I, (V-I)_0$ CMD of Hoyt (2023) compared with those from Rizzi et al. (2007) (dashed line) and updated by Jang & Lee (2017a) (dot-dashed line). Note that the TRGB loci of the LMC and SMC are in excellent agreement with that of Jang & Lee (2017a) with updated zero points.

Figure 7 illustrates the absolute $I$-band magnitude of the TRGB as a function of year of publication. Since the earlier calibrations (Mould et al. 1983; Lee et al. 1993), numerous calibrations based on various methods have been presented. Calibration sources are diverse: Milky Way globular clusters, Local Group galaxies, as well as the LMC and SMC, NGC 4258, *Gaia* stars in the Milky Way, and theoretical models. Most of the new

https://doi.org/10.1017/S1743921323002685 Published online by Cambridge University Press

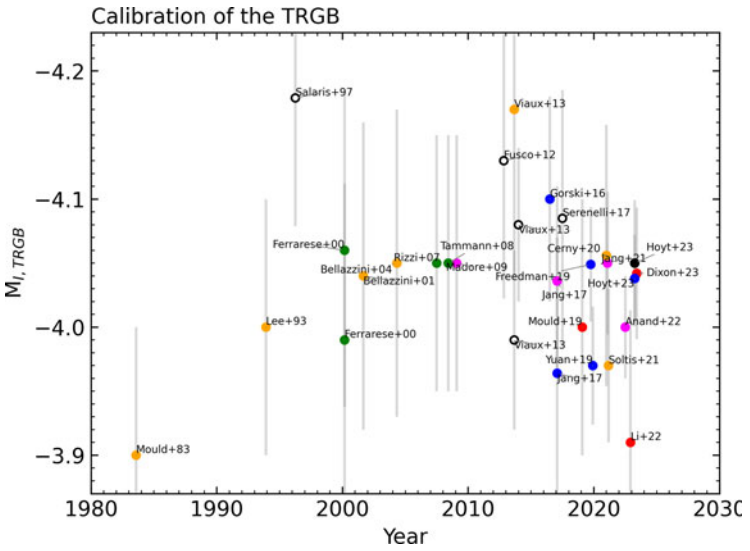


**Figure 7.** TRGB $I$-band magnitude calibration as a function of year of publication. Different symbols represent the calibration sources: yellow circles for Milky Way globular clusters, green circles for Local Group galaxies, blue circles for the LMC, black circles for the SMC, pink circles for NGC 4258, red circles for *Gaia* stars in the Milky Way, and open circles for theoretical models. (Prepared by In Sung Jang).

calibrations are consistent with the old value of Lee et al. (1993), $M_I = -4.0 \pm 0.1$ mag. However, the calibration errors are gradually becoming smaller, to the level of $\pm 0.05$ mag, or even smaller. Note that Freedman (2021) derived $M_I = -4.049 \pm 0.015(\text{stat.}) \pm 0.035(\text{syst.})$ mag from a sample of four distance anchors: Milky Way globular clusters, LMC, SMC, and NGC 4258. This value is very similar to those of Jang et al. (2021) and Hoyt (2023). Interestingly, the two recent values derived from *Gaia* Data Release 3 of TRGB stars in the Milky Way (Li et al. 2022; Dixon et al. 2023) show a 0.1 mag difference. Although the Dixon et al. (2023)'s value is consistent with others discussed here, the Li et al. (2022) value is found at the faintest end.

In summary, it is reasonable to adopt the TRGB magnitude calibration for low-metallicity systems, $M_I = -4.05 \pm 0.05$ mag, as well as the TRGB locus of Jang & Lee (2017a), with the updated zero point, as shown in Figure 6. It is expected that the accuracy of the TRGB magnitude will become even better in the near future.

## 3. TRGB Science Cases

### 3.1. *The Hubble Flow with SNe Ia*

SNe Ia are a powerful standard(izable) candle for measuring the expansion history of the Universe. The first step in the SNe Ia cosmology is to calibrate the peak magnitude of SNe Ia using nearby SNe Ia host galaxies with known distances. Cepheids used to be the most popular tool for SNe Ia calibration. Note that the TRGB is another excellent candle for SNe Ia calibration and that SNe Ia are found not only in late-type but also in early-type galaxies. At present, the distance ladder to derive the value of the Hubble constant in supernova cosmology has become much simpler than in the past, as shown in Figure 8.

Figure 9 shows the evolution of the measured values of the local Hubble constant derived from Cepheid-calibrated SNe Ia since 2000 (blue symbols), in comparison with the values derived from extrapolation of the cosmic microwave background radiation (CMBR) measurements (black, yellow, and green symbols) (Freedman 2021). The value

https://doi.org/10.1017/S1743921323002685 Published online by Cambridge University Press

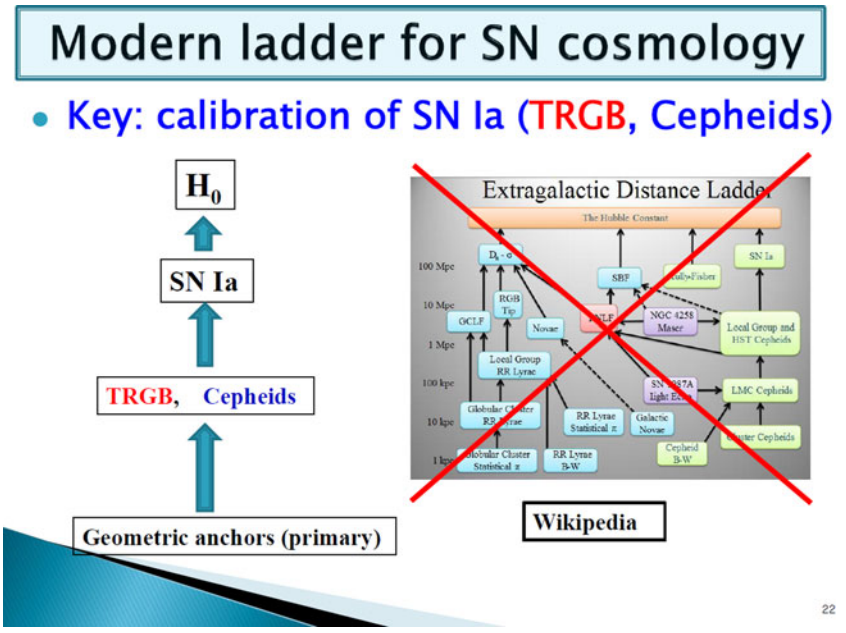


**Figure 8.** Modern distance ladder for supernova cosmology. Note that the TRGB and Cepheids are calibrated directly using geometric distance anchors. Currently, they are two major standard candles to calibrate SNe Ia.

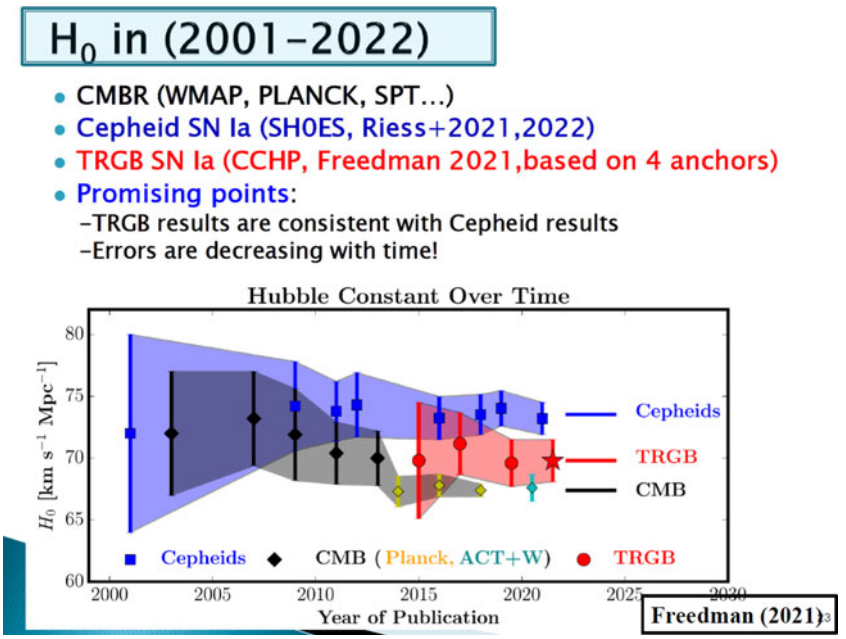


**Figure 9.** Comparison of local $H_0$ measurements derived from three methods: Cepheid-calibrated SNe Ia (blue symbols), TRGB-calibrated SNe Ia (red symbols), and the CMBR (black, yellow, and green symbols) (Freedman 2021).

https://doi.org/10.1017/S1743921323002685 Published online by Cambridge University Press

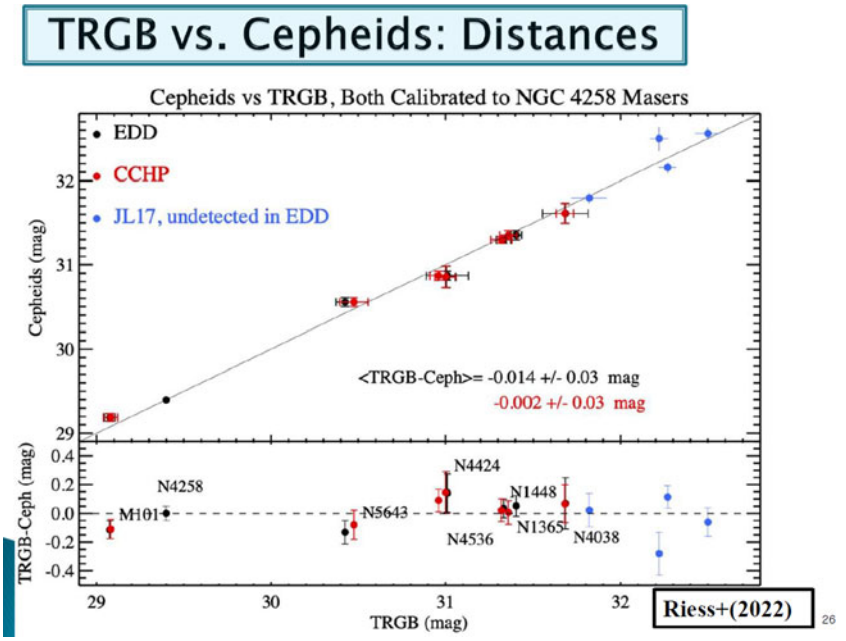


**Figure 10.** Comparison of TRGB and Cepheid distances to the same galaxies (Riess et al. 2022). The TRGB distances are from the CCHP (Freedman 2021, red symbols), EDD (Anand et al. 2021, black symbols), and TIPSNU for the most distant galaxies (Jang & Lee 2017b, blue symbols).

of the local Hubble constant derived from Cepheid-calibrated SNe Ia (Riess et al. 2021, 2022) is larger than the value extrapolated from the CMBR, at the level of 5–6$\sigma$. This problem is referred to as the 'Hubble tension'. It is one of the hottest topics in present-day cosmology (see Perivolaropoulos & Skara 2022, and references therein).

Figure 9 also shows recent measurements of the Hubble constant derived from TRGB-calibrated SNe Ia (Jang & Lee 2017b; Freedman et al. 2019; Freedman 2021), in red symbols. The TRGB-calibrated $H_0$ from Freedman (2021) is slightly larger than the CMBR value, while it is slightly smaller than the Cepheid-calibrated value (Riess et al. 2022). The differences are at the level of 2$\sigma$, showing little tension with either of the two measurements. Note also that the measurement errors from each method are, on average, decreasing as time passes. We expect that the errors will become even smaller in the near future.

Figure 10 displays a comparison of TRGB and Cepheid distances to the same galaxies given by Riess et al. (2022) (see also Anand et al. (2022)). The TRGB distances are from the Carnegie–Chicago Hubble Program (CCHP; Freedman 2021, red symbols), the Extragalactic Distance Database (EDD) for nearby galaxies (Anand et al. 2021, black symbols), and the Tip of the RGB for SN host galaxies in the Universe (TIPSNU) for the most distant galaxies (Jang & Lee 2017b, blue symbols). Note that Anand et al. (2021) provided a very useful catalog of TRGB distances in the EDD, but the galaxies in their catalog are located at $d < 20$ Mpc. TRGB distances to more distant galaxies are given by Jang & Lee (2017b). All these distances were calibrated with respect to the NGC 4258 maser distance for this comparison. The TRGB distances from these three different projects all show remarkable agreement with the Cepheid distances.

https://doi.org/10.1017/S1743921323002685 Published online by Cambridge University Press

### 3.2. *Virgo Cluster Infall and Dark Matter*

While the motion of galaxies in low-density environments follow the Hubble flow, the motion of galaxies around galaxy clusters/groups is affected by the combination of the local gravity and the Hubble flow. Thus, the galaxies around galaxy clusters/groups are useful for estimating not only the local dark matter distribution but also the value of the Hubble constant. Assuming a spherical shell of radius $R$ moving radially in a cluster with mass $M$, the motions of galaxies near the cluster in a Universe with $\Omega_\Lambda$ can be described as (Peirani & de Freitas Pacheco 2006, 2008):

$$\frac{\mathrm{d}^2R}{\mathrm{d}t^2} = -\frac{GM}{R^2} + \Omega_\Lambda \mathrm{H}_0^2 R. \tag{1}$$

Solving this equation, we can derive $\mathrm{H}_0$ and $M_0(R_0)$, where $R_0$ is the radius of the zero-velocity surface of the cluster and $M_0$ is the cluster mass within the zero-velocity radius. The clustercentric velocity $V_\mathrm{C}$ is given in terms of $M(R)$ and $\mathrm{H}_0$, as (with the *Planck* value of $\Omega_\Lambda = 0.685$ and $n \sim 0.7$):

$$V_\mathrm{C}(R) = -\frac{0.940\mathrm{H}_0}{R^n}\left(\frac{GM}{\mathrm{H}_0^2}\right)^{(n+1)/3} + 1.335\mathrm{H}_0 R. \tag{2}$$

The cluster mass, $M_0$, is given in terms of $R_0$ and $\mathrm{H}_0$ as:

$$M_0 = \frac{1.855}{G} \times \mathrm{H}_0^2 R_0^3 = 4.29 \times 10^{12} h_{100}^2 \left(\frac{R_0}{[\mathrm{Mpc}]}\right)^3 \mathrm{M}_\odot. \tag{3}$$

The Virgo Cluster, the nearest galaxy cluster, is an excellent laboratory where we can apply this method. In this regard, the galaxies located between the Virgo Cluster and the Milky Way play an important role (Karachentsev et al. 2018; Kashibadze & Karachentsev 2018; Kashibadze et al. 2020). It is expected that these galaxies are subject to infall into the Virgo Cluster center. The TRGB is the best standard candle to measure the distances to these infalling galaxies. Kim et al. (2020) used the kinematics of 33 galaxies with TRGB distances (McQuinn et al. 2014, 2017; Karachentsev et al. 2018; Kim et al. 2020; Tikhonov & Galazutdinova 2020) in front of the Virgo Cluster. Figure 11 shows the locations and line-of-sight velocities of these galaxies. Most are located in the northern region of Virgo, and only four galaxies are in the southern volume of the Virgo Cluster.

The virgocentric velocity of each infalling galaxy was derived from the observed line-of-sigh velocity and the separation angular distance with respect to the Virgo center (assuming a radial velocity of $v = 988$ km s$^{-1}$ at a distance of 16.5 Mpc; Kashibadze et al. 2020). Following Kashibadze & Karachentsev (2018) and Kashibadze et al. (2020), Virgocentric velocities of infalling galaxies were derived for two extreme cases, i.e., a minor attractor model where the peculiar motion is negligible compared with the Hubble flow, and a major attractor model where the peculiar motion is comparable to the Hubble flow.

Figure 12 displays the Hubble diagram, showing the Virgocentric velocity versus Virgocentric distance of the infalling galaxies. Fitting the data with the above models and taking a mean of the two model results, Kim et al. (2020) derived a value of the local Hubble Constant, $\mathrm{H}_0 = 65.9 \pm 3.5(\mathrm{stat.}) \pm 2.4(\mathrm{syst.})$ km s$^{-1}$ Mpc$^{-1}$. This value for $\mathrm{H}_0$ is consistent with the value derived independently from the TRGB-calibrated SNe Ia, although its error is larger than the latter: see Figure 13.

The zero-velocity radius is derived as $R_0 = 6.76 \pm 0.35$ Mpc, and the corresponding mass is $M_0(< R_0) = (5.7 \pm 1.5) \times 10^{14}$ M$_\odot$. The virial radius and mass of Virgo are $R_{200} = 1.7$ Mpc and $M_\mathrm{vir} = (4\text{–}6) \times 10^{14}$M$_\odot$, respectively (Kashibadze et al. 2020). This confirms that the dark matter content of the Virgo Cluster is mostly located inside the

https://doi.org/10.1017/S1743921323002685 Published online by Cambridge University Press

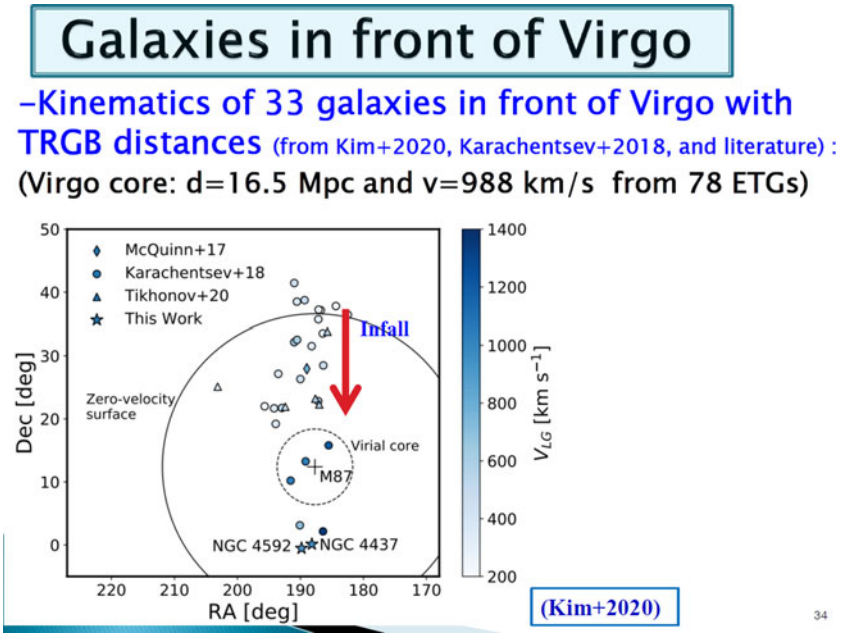


**Figure 11.** Locations of the galaxies in front of the Virgo Cluster (Kim et al. 2020). The color bar represents the line-of-sight velocity of each galaxy with respect to the center of the Local Group.

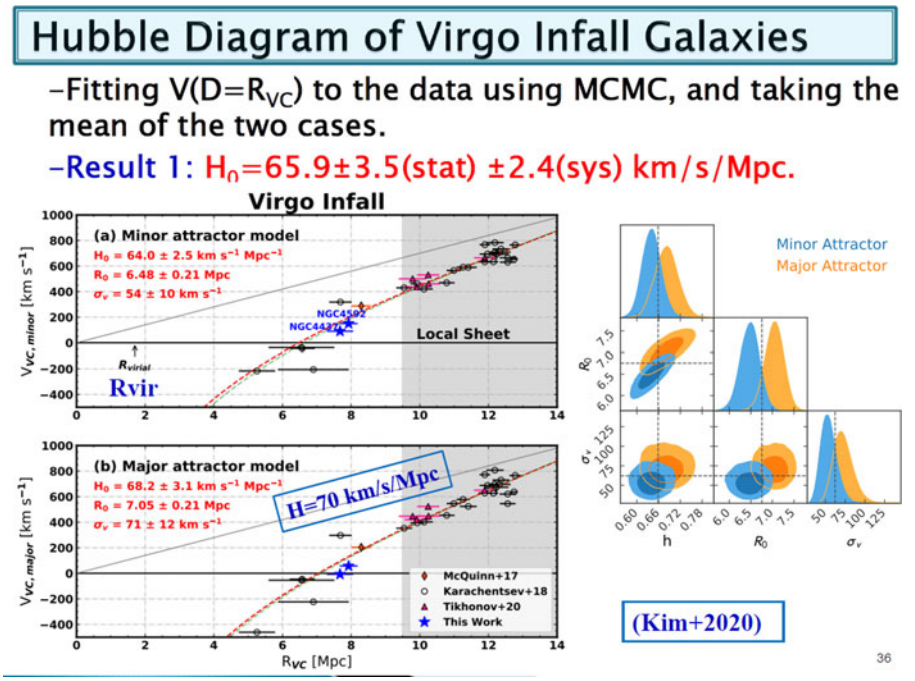


**Figure 12.** Hubble diagram of the Virgo infall galaxies showing Virgocentric velocity versus Virgocentric distance for the minor (top) and major (bottom) attractor models. The red dashed lines denote the model fits. The right panels show the posterior probability distributions for the fitted parameters, $h$, $R_0$, and $\sigma_v$. The blue and yellow colors represent the minor and major attractor models, respectively (Kim et al. 2020).

https://doi.org/10.1017/S1743921323002685 Published online by Cambridge University Press

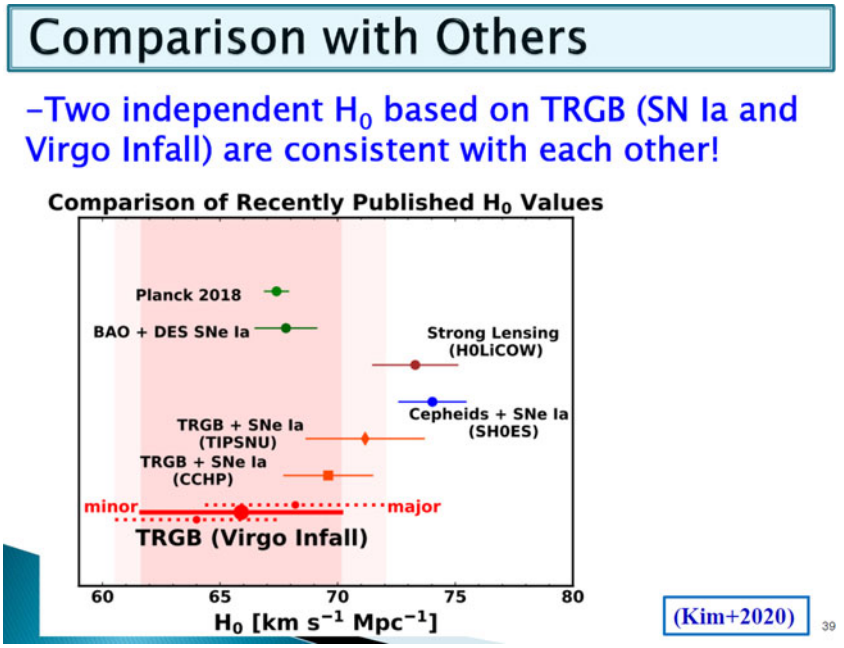


**Figure 13.** Comparison of the Hubble constants derived from the Virgo infall galaxies and other methods (Kim et al. 2020).

virial radius and that the fraction of dark matter between the virial radius and the zero-velocity radius is negligible (Karachentsev et al. 2018; Kashibadze et al. 2020).

In addition, the velocity dispersion of the infalling galaxies is estimated at $\sigma_0 = 62 \pm 14$ km s$^{-1}$. This is even smaller than the value given by Karachentsev et al. (2018), $\sigma_0 = (78–90)$ km s$^{-1}$. This confirms that the Hubble flow around the Virgo Cluster is cold (Kashibadze & Karachentsev 2018; Karachentsev et al. 2018).

### 3.3. *Dark Galaxies?*

Dark galaxies are isolated HI systems with barely visible optical counterparts. They are usually found in HI surveys (Cannon et al. 2015; Ball et al. 2018, and references therein). They can be either real galaxies or simply gas fragments in the Milky Way. Their origin is not clear. Some of them are associated with a low surface brightness (LSB) stellar system, which provides a critical clue to understand their origin. It is not easy to determine a distance to these LSB systems. If we know their distances, we can derive their physical properties and tell whether they are galaxies or gas clouds in the Milky Way. The TRGB is an excellent tool to measure the distances to these dark galaxies with LSB counterparts and investigate the nature of dark galaxies.

Coma P is an enigmatic example of an almost dark galaxy: an LSB optical counterpart is located at the location of AGC 229385, a large HI system with $v = 1348$ km s $^{-1}$ (Janowiecki et al. 2015; Ball et al. 2018). Figure 14 shows an HI contour map and a color map based on *HST*/Advanced Camera for Surveys (ACS) F606W/F814W images of AGC 229385/Coma P (Ball et al. 2018).

TRGB distances to Coma P derived from the same *HST*/ACS images have been controversial, often showing large differences (Anand et al. 2018; Brunker et al. 2019; Tikhonov & Galazutdinova 2020). Figure 15 displays the CMDs of the detected stars in the *HST*/ACS F606W/F814W images of Coma P from different authors. Anand et al.

https://doi.org/10.1017/S1743921323002685 Published online by Cambridge University Press

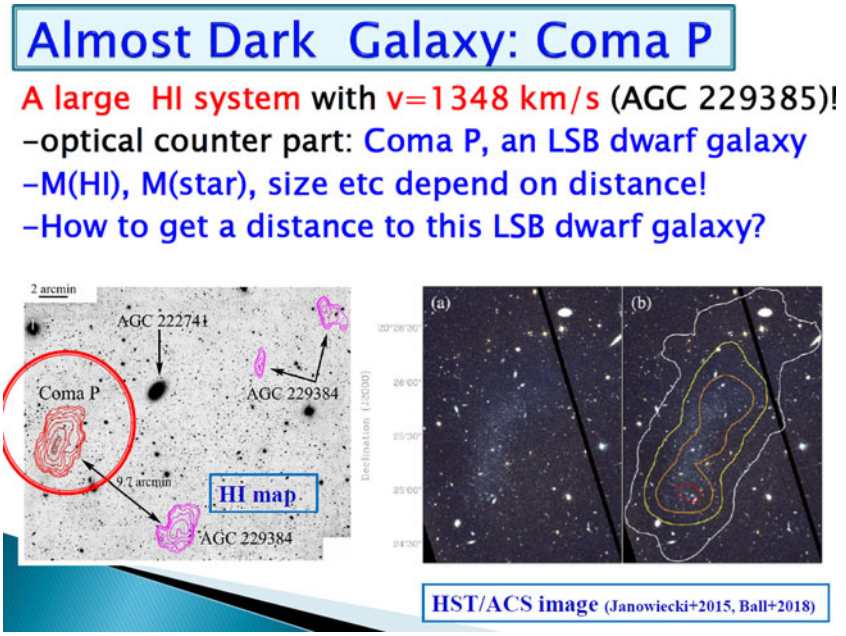


**Figure 14.** (left) HI map of AGC 229385/Coma P (red contours). (right) Color map of the *HST*/ACS images of Coma P. White contours represent the number density of detected stars in the *HST* images of Coma P, clearly showing the existence of a galaxy (Ball et al. 2018).

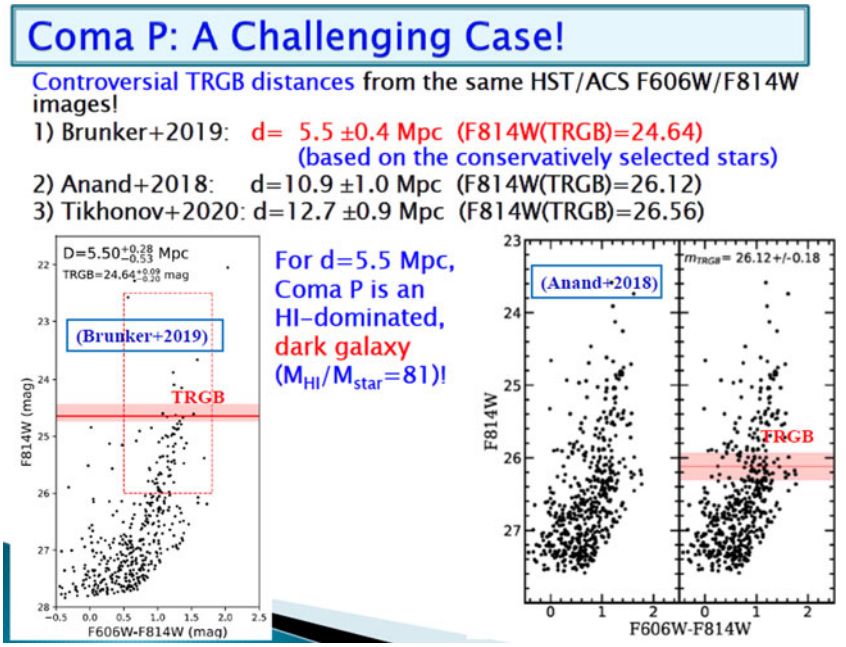


**Figure 15.** CMDs of the detected stars in the *HST*/ACS images of Coma P from Brunker et al. (2019) (left) and Anand et al. (2018). Note that the loci of the TRGB in the two CMDs are significantly different.

https://doi.org/10.1017/S1743921323002685 Published online by Cambridge University Press

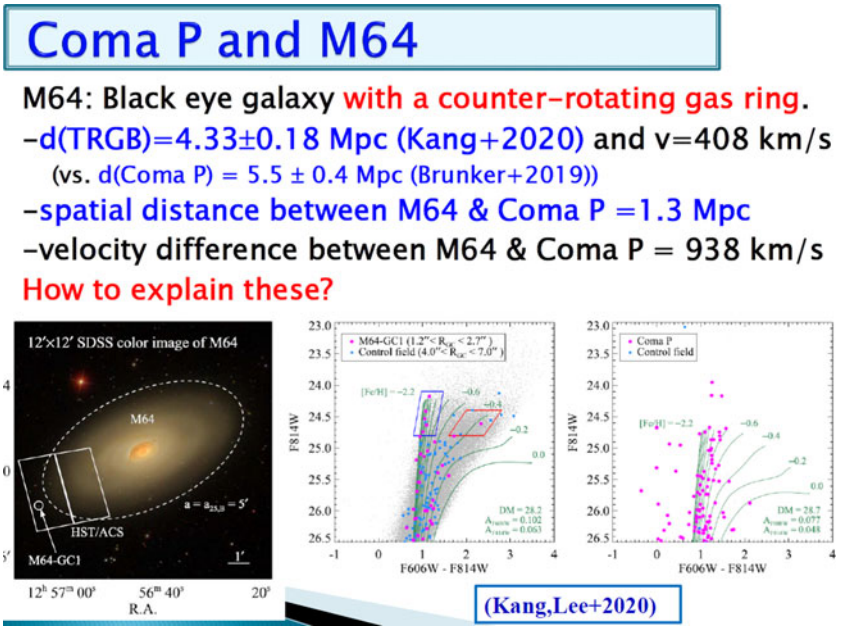


**Figure 16.** Relation between Coma P and M64. (left) SDSS color image of M64. The boxes denote the *HST*/ACS field. (middle) CMD of the detected stars in the *HST* images of M64 (gray dots). Magenta circles represent stars in the globular cluster M64-GC1 and blue circles are stars in the control field around the globular cluster. Green lines denote the PARSEC isochrones for an age of 12 Gyr and [Fe/H] = −2.2 to 0.0 dex (Bressan et al. 2012). (right) CMD of the detected stars in the *HST*/ACS images of Coma P (magenta circles). (Kang et al. 2020).

(2018) derived F814W(TRGB) = 26.12 mag and $d = 10.9 \pm 1.0$ Mpc. Then, selecting their sample stars more conservatively, Brunker et al. (2019) suggested that the TRGB magnitude is 1.5 mag brighter than the Anand et al. (2018) value, F814W(TRGB) = 24.64 mag, yielding a much shorter distance, $d = 5.5 \pm 0.4$ Mpc. Later, Tikhonov & Galazutdinova (2020) adopted the outer region of Coma P to measure the TRGB, obtaining an 0.4 mag fainter value than Anand et al. (2018), F814W(TRGB) = 26.56 mag (and $d = 12.7 \pm 0.9$ Mpc). Visual inspection of the CMDs in these references indicates that the Brunker et al. (2019) value may be the most persuasive. However, better *HST* data are needed to resolve this problem. These results show that Coma P is a difficult example for TRGB application.

For the distance to Coma P of Brunker et al. (2019), the ratio of the HI and stellar mass is derived as large as 81, showing that Coma P is indeed an HI-dominated dark galaxy. Coma P is located in a sparse field, and the nearest galaxy from Coma P in the sky is M64 (the Black Eye galaxy), an early-type SA spiral galaxy. Figure 16 displays the Sloan Digital Sky Survey (SDSS) color image of M64, where the position of one *HST*/ACS field is marked on the eastern side of M64. One interesting feature of M64 is the presence of a counter-rotating HI gas ring.

Kang et al. (2020) discovered one bright globular cluster, M64-GC1, in the *HST* field of M64 and showed that it is a metal-poor globular cluster in the halo of M64 based on the CMD of the detected globular cluster stars (see Figure 16, middle). They compared the CMDs of the resolved stars in M64-GC1 and Coma P (see Figure 16, right), showing that the mean metallicity of Coma P is [Fe/H] ≈ −0.9 dex, which is slightly higher than that of M64-GC1, [Fe/H] = −1.5 ± 0.2 dex.

https://doi.org/10.1017/S1743921323002685 Published online by Cambridge University Press

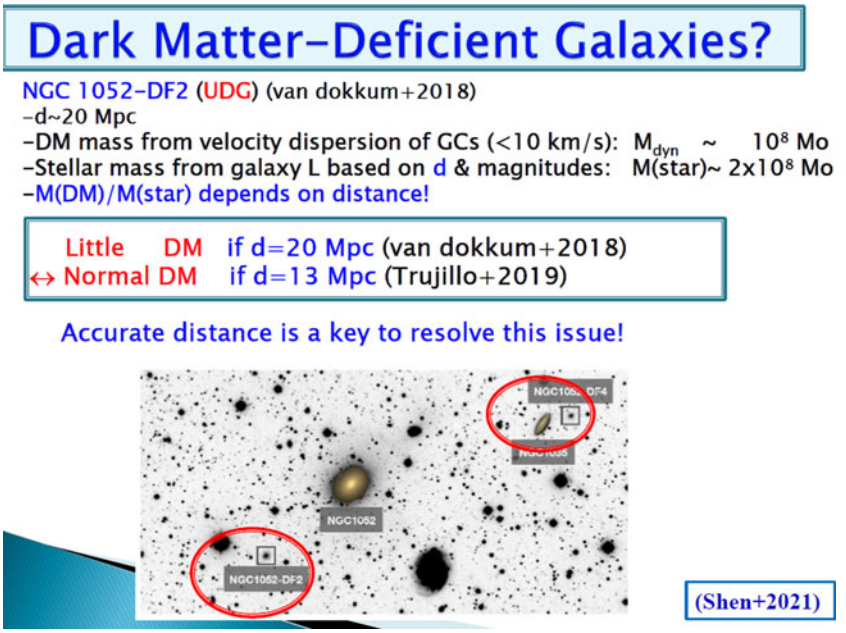


**Figure 17.** Locations of NGC 1052-DF2 and NGC 1052-DF4, both members of the NGC 1052 group (Shen et al. 2021).

Kang et al. (2020) derived a TRGB distance to M64 ($d = 4.44 \pm 0.18$ Mpc), showing that it is at the spatial distance of 1.3 Mpc from Coma P. However, the relative velocity of Coma P with respect to M64 is as large as $\Delta v = 938$ km s$^{-1}$. This can be explained in terms of a high-speed flyby scenario: a gas-rich massive progenitor of Coma P encountered M64 at high speed about one giga-year ago, and some of the gas removed from Coma P resulted in the counter-rotating gas ring in the outer disk of M64 (Brunker et al. 2019; Kang et al. 2020).

### 3.4. *Dark Matter-free Galaxies?*

The current paradigm for galaxy formation models is based on the assumption that the baryonic components of galaxies are embedded in much larger and more massive dark matter halos. Are there any galaxies whose dark matter fraction is significantly lower than for normal galaxies? If so, they must be large galaxies with very low surface brightness (also dubbed 'ultra-diffuse galaxies', UDGs). They are called dark matter-free (or dark matter-deficient) galaxies. NGC 1052-DF2 ([KKK2000]04), a UDG in the NGC 1052 group, is a strong candidate for such dark matter-free galaxies. Figure 17 shows the location of NGC 1052-DF2 in the NGC 1052 group (Shen et al. 2021).

van Dokkum et al. (2018) estimated the dynamical mass of NGC 1052-DF2, from the kinematics of its globular clusters, $M_{\rm dyn} \sim 10^8 {\rm M}_\odot$. They also derived a twice larger stellar mass for this galaxy, $M_* \sim 2 \times 10^8 {\rm M}_\odot$, adopting a distance of 20 Mpc. Based on these results, they suggested that NGC 1052-DF2 may be a dark matter-deficient galaxy. Later, Trujillo et al. (2019) derived a much closer distance to this galaxy, $d = 13$ Mpc, thus claiming that NGC 1052-DF2 is a normal galaxy. However, the *HST* images used for these studies are not deep enough to derive a reliable distance to this galaxy. Access to an accurate distance is key to resolving this issue. The TRGB is an excellent tool to measure the distance to these LSB galaxies and tell us whether or not they are dark matter-deficient.

https://doi.org/10.1017/S1743921323002685 Published online by Cambridge University Press

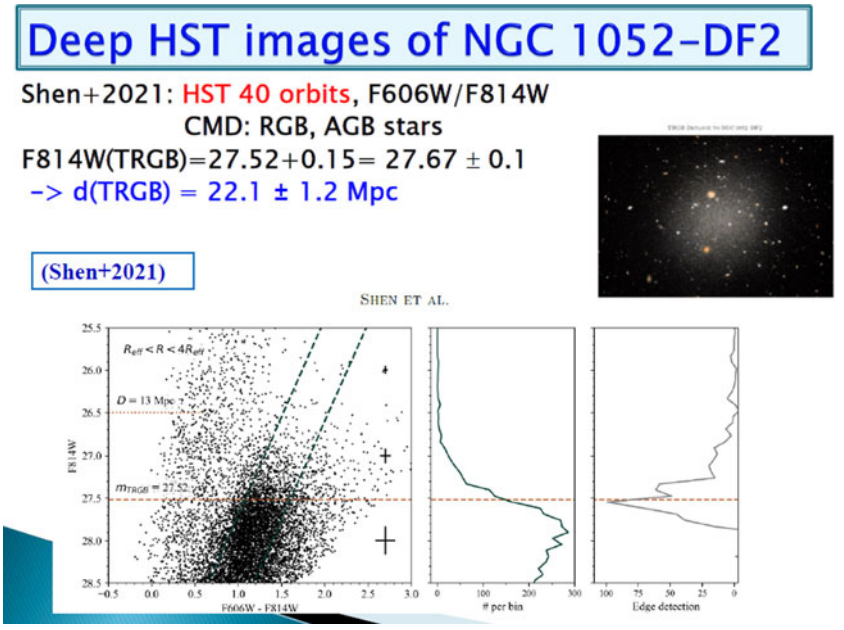


**Figure 18.** (top) Color map of the *HST* images of NGC 1052-DF2. (bottom) CMD, LF, and edge detector response of the detected stars in NGC 1052-DF2. The red dashed line denotes the locus of the TRGB (Shen et al. 2021).

Later, using much deeper *HST*/WFC3 F606W/F814W images, Shen et al. (2021) obtained much better photometry of the resolved stars in NGC 1052-DF2 and measured the TRGB magnitude and distance, F814W(TRGB) $= 27.67 \pm 0.1$ mag and $d = 22.1 \pm 1.2$. Figure 18 displays the CMD of the detected stars in NGC 1052-DF2, the LF of the selected RGB stars, and the corresponding edge detector response (Shen et al. 2021). The TRGB distance derived from the deeper *HST* images is consistent with the result of van Dokkum et al. (2018), showing that NGC 1052-DF2 is indeed a dark matter-deficient galaxy. Similarly, Danieli et al. (2020) derived a TRGB distance to NGC 1052-DF4, $d = 20. \pm 1.6$ Mpc, showing that it is another member of the NGC 1052 group and that it is also a dark matter-deficient galaxy. The presence of these dark matter-deficient galaxies can be explained by high-speed collisions of two gas-rich dwarfs or tidal stripping (Silk 2019; Lee et al. 2021; van Dokkum et al. 2022).

## 4. Summary and Outlook

The TRGB is the best standard candle for the cosmology of the local Universe. The accuracy of the TRGB continues to be improved. I have introduced four TRGB science cases, from large to small scales. However, they are only a small fraction of the possible science cases, and there are many more interesting cosmological projects one can do with the TRGB.

The *HST* has been a major workhorse for TRGB science since 1990. In 2022, the *JWST* started science observations, opening up a new era in near/mid-infrared high resolution imaging. The Vera Rubin Observatory/Legacy Survey of Space and Time will start operations soon from the ground, and the Nancy Roman Space Telescope will provide the wide-field, high-resolution space-borne imaging in a few years' time. Better spatial resolution, infrared coverage, and the wider fields of current and future telescopes will expand the TRGB reach from 30 Mpc to 100 Mpc, and also expand the TRGB sky

https://doi.org/10.1017/S1743921323002685 Published online by Cambridge University Press

coverage, filling a significant fraction of the sky. Let us enjoy TRGB cosmology in the forthcoming years!

**Acknowledgements.** Thanks to In Sung Jang for preparing some figures. This work was supported by a National Research Foundation grant funded by the Korean Government (NRF-2019R1A2C2084019).

## References

Anand, G. S., Tully, R. B., Karachentsev, I. D., Makarov, D. I., Makarova, L., Rizzi, L., Shaya, Edward J. 2018, ApJL, 861, L6. doi:10.3847/2041-8213/aacc2b
Anand, G. S., et al. 2021, AJ, 162, 80. doi:10.3847/1538-3881/ac0440
Anand, G. S., Tully, R. B., Rizzi, L., Riess, A. G.; Yuan, W. 2022, ApJ, 932, 15. doi:10.3847/1538-4357/ac68df
Baade, W. 1944, ApJ, 100, 137. doi:10.1086/144650
Ball, C., et al. 2018, AJ, 155, 65. doi:10.3847/1538-3881/aaa156
Beaton, R. L., et al. 2019, Astronomical Distance Determination in the Space Age. Series: Space Sciences Series of ISSI, 89. doi:10.1007/978-94-024-1631-2_4
Bellazzini, M. 2008, Mem. Soc. Astron. It., 79, 440. doi:10.48550/arXiv.0711.2016
Bressan, A., Marigo, P., Girardi, L., Salasnich, Bernardo; Dal Cero, C;, Rubele, S., Nanni, A. 2012, MNRAS, 427, 127. doi:10.1111/j.1365-2966.2012.21948.x
Brunker, et al. 2019, AJ, 157, 76. doi:10.3847/1538-3881/aafb39
Cannon, J. M., et al. 2015, AJ, 149, 72. doi:10.1088/0004-6256/149/2/720049/198/1/6
Danieli, S., van Dokkum, P., Abraham, R., Conroy, C., Dolphin, A. E., Romanowsky, A. J. 2020, ApJL, 895, L4. doi:10.3847/2041-8213/ab8dc4
Dixon, M., Mould, J., Flynn, C., et al. 2023, MNRAS, 523, 2283. doi:10.1093/mnras/stad1500
Freedman, W. L., Hatt, D., et al. 2019, ApJ, 882, 34. doi:10.3847/1538-4357/ab2f73
Freedman, W. L., et al. 2020, ApJ, 891, 57. doi:10.3847/1538-4357/ab7339
Freedman, W. L. 2021, ApJ, 919, 16. doi:10.3847/1538-4357/ac0e95
Hatt, D., et al. 2017, ApJ, 845, 146. doi:10.3847/1538-4357/aa7f73
Hoyt, T. J. 2023, Nat. Astron., 7, 590. doi:10.1038/s41550-023-01913-1
Jang, I. S. & Lee, M. G. 2017a, ApJ, 835, 28. doi:10.3847/1538-4357/835/1/28
Jang, I. S. & Lee, M. G. 2017b, ApJ, 836, 74. doi:10.3847/1538-4357/836/1/74
Jang, I. S., et al. 2021, ApJ, 906, 125. doi:10.3847/1538-4357/abc8e9
Janowiecki, S., et al. 2015, ApJ, 801, 96
Kang, J., Kim, Y. J., Lee, M. G., Jang, I. S. 2020, ApJ, 897, 106. doi:10.3847/1538-4357/ab94ba
Karachentsev, I. D., Makarova, L. N., Tully, R. B., Rizzi, L., Shaya, E. J. 2018, ApJ, 858, 62. doi:10.3847/1538-4357/aabaf1
Kashibadze, O. G. & Karachentsev, I. D. 2018, A&A, 609, A11. doi:10.1051/0004-6361/201731645
Kashibadze, O. G., Karachentsev, I. D., & Karachentseva, V. E. 2020, A&A, 635, A135. doi:10.1051/0004-6361/201936172
Kim, Y. J., Kang, J., Lee, M. G., Jang, I. S. 2020, ApJ, 905, 104. doi:10.3847/1538-4357/abbd97
Lee, M. G. 1993, ApJ, 408, 409. doi:10.1086/172598
Lee, M. G., Freedman, W. L., & Madore, B. F. 1993, ApJ, 417, 553. doi:10.1086/173334
Lee, J., Shin, E.-. jin., & Kim, J.-h. 2021, ApJL, 917, L15. doi:10.3847/2041-8213/ac16e0
Li, S., Casertano, S., & Riess, A. G. 2022, ApJ, 939, 96. doi:10.3847/1538-4357/ac7559
Madore, B. F., Mager, V., & Freedman, W. L. 2009, ApJ, 690, 389. doi:10.1088/0004-637X/690/1/389
Madore, B. F., Freedman, W. L., Owens, K. A., Jang, I. S. 2023, AJ, 166, 2. doi:10.3847/1538-3881/acd3f3
Makarov, D., Makarova, L., Rizzi, L., Tully, R. Brent; Dolphin, A. E., Sakai, S., Shaya, E. J. 2006, AJ, 132, 2729. doi:10.1086/508925
McQuinn, K. B. W., et al. 2014, ApJ, 785, 3. doi:10.1088/0004-637X/785/1/3
McQuinn, K. B. W., Skillman, E. D., Dolphin, A. E., Berg, D., Kennicutt, R. 2017, AJ, 154, 51. doi:10.3847/1538-3881/aa7aad

Méndez, B., Davis, M., Moustakas, J., Newman, J., Madore, B. F., Freedman, W. L. 2002, AJ, 124, 213. doi:10.1086/341168
Mould, J. R., Kristian, J., & Da Costa, G. S. 1983, ApJ, 270, 471. doi:10.1086/161141
Mould, J., Clementini, G., & Da Costa, G. 2019, PASA, 36, e001. doi:10.1017/pasa.2018.46
Peirani, S., & de Freitas Pacheco, J. A. 2006, New Astron., 11, 325
Peirani, S., & de Freitas Pacheco, J. A. 2008, A&A, 488, 845
Perivolaropoulos, L. & Skara, F. 2022, New Astron. Rev., 95, 101659. doi:10.1016/j.newar.2022.101659
Riess, A. G., Casertano, S., Yuan, W., Bowers, J. B., Macri, L., Zinn, J. C., Scolnic, D. 2021, ApJL, 908, L6. doi:10.3847/2041-8213/abdbaf
Riess, A. G., et al. 2022, ApJL, 934, L7. doi:10.3847/2041-8213/ac5c5b
Rizzi, L., Tully, R. B., Makarov, D., Makarova, Lidia; Dolphin, A. E., Sakai, S., Shaya, E. J. 2007, ApJ, 661, 815. doi:10.1086/516566
Salaris, M. & Cassisi, S. 1997, MNRAS, 289, 406. doi:10.1093/mnras/289.2.406
Serenelli, A., Weiss, A., Cassisi, S., Salaris, M., Pietrinferni, A. 2017, A&A, 606, A33. doi:10.1051/0004-6361/201731004
Shen, Z., et al. 2021, ApJL, 914, L12. doi:10.3847/2041-8213/ac0335
Silk, J. 2019, MNRAS, 488, L24. doi:10.1093/mnrasl/slz090
Soltis, J., Casertano, S., & Riess, A. G. 2021, ApJL, 908, L5. doi:10.3847/2041-8213/abdbad
Tammann, G. A., Sandage, A., & Reindl, B. 2008, ApJ, 679, 52. doi:10.1086/529508
Tikhonov, N. A. & Galazutdinova, O. A. 2020, Astron. Lett., 45, 750. doi:10.1134/S1063773719110069
Trujillo, I., et al. 2019, MNRAS, 486, 1192. doi:10.1093/mnras/stz771
Tully, R. B., et al. 2023, ApJ, 944, 94. doi:10.3847/1538-4357/ac94d8
van Dokkum, P., et al. 2018, ApJL, 864, L18. doi:10.3847/2041-8213/aada4d
van Dokkum, P., et al. 2022, Nature, 605, 435. doi:10.1038/s41586-022-04665-6